

Čerenkov nonlinear diffraction of femtosecond pulses

A. M. Vyunishev,^{1,2,*} A. S. Aleksandrovsky,^{1,2} A. I. Zaitsev,^{1,2} and V. V. Slabko²

¹*L.V. Kirensky Institute of Physics, 660036 Krasnoyarsk, Russia*

²*Siberian Federal University, 660079 Krasnoyarsk, Russia*

*Corresponding author: vyunishev@iph.krasn.ru

Received April 2, 2013; revised June 4, 2013; accepted June 4, 2013;
posted June 5, 2013 (Doc. ID 188104); published June 28, 2013

Čerenkov nonlinear diffraction of femtosecond pulses in one-dimensional nonlinear photonic crystal of strontium tetraborate was studied theoretically and experimentally in both frequency and time domains. Spectral features of second harmonic radiation were measured in the course of mapping the nonlinear photonic crystal structure. The local second harmonic spectrum demonstrates complex angular behavior within the beam cross section. The spectral width of the second harmonic radiation is found to be fundamental beam size-dependent, and optimal focusing should be used for exact conversion of the fundamental spectrum into the second harmonic one. Experimental results are in excellent agreement with calculations. Maximum second harmonic generation efficiency was up to 2.1% at pumping by a femtosecond oscillator. © 2013 Optical Society of America

OCIS codes: (190.0190) Nonlinear optics; (190.2620) Harmonic generation and mixing; (190.7110) Ultrafast nonlinear optics; (160.4330) Nonlinear optical materials.

<http://dx.doi.org/10.1364/JOSAB.30.002014>

1. INTRODUCTION

Spatial modulation of second-order nonlinear susceptibility is known to be an efficient way to achieve phase matching in frequency conversion processes. Nonlinear media employing this modulation are called nonlinear photonic crystals (NPCs) [1]. These media are found to be useful for multicolor [2–4] and multidirectional [5,6] frequency conversion, biphoton [7,8] and terahertz [9] generation, wavefront engineering [10], etc. One of the most studied phenomena realized in NPCs is nonlinear diffraction, discovered by Freund in a ferroelectric domain structure [11]. Reciprocal lattice vectors (RLVs) of these structures allow one to match transverse components of the harmonic wave vectors involved, while longitudinal components are strictly matched under a Čerenkov-type phase matching condition that is observed in waveguides and films [12,13] and results in Čerenkov nonlinear diffraction (CND). A perfect case of CND can be observed in bulk media [14]. Simultaneous fulfillment of both conditions results in a perfect case of nonlinear Bragg diffraction (NBD), the angular properties of which, as one must expect, coincide with the Čerenkov condition. An intermediate case must take place in periodic NPC with a mismatch from the exact transversal condition or in a random NPC [15–20]. It can be treated as a case of CND affected by nonlinear susceptibility modulation. Interesting results were obtained with nonlinear diffraction in a medium with a single domain wall [21–25]. This case must be closer to a perfect CND. High sensitivity to nonlinear susceptibility modulation makes CND a powerful tool for ferroelectric domain study and its visualization [26,27]. Dispersion of most ferroelectric crystals is relatively high and does not allow CND in the visible and near-IR using the first order of transverse component matching at actual abilities of the poling technology, restricting conversion efficiency [28,29]. Use of higher order matching leads to a decrease in CND conversion efficiency. It has recently been shown [30] that

conversion efficiency in periodically poled nonlinear crystals can be remarkably enhanced by angular tuning because of lower orders, but the oblique incidence of the fundamental frequency (FF) beam leads to symmetry breaking of both power and propagation directions of specific second harmonic (SH) beams with respect to the fundamental one. For this reason efficient CND with a symmetric distribution of SH power is supposed to require nonlinear crystals with low dispersion. An example of such crystal is strontium tetraborate (SBO), which demonstrates the ability for one-dimensional (1D) spontaneous domain structures to be formed. Domain thickness in SBO is highly randomized and may be as thin as 100 nm. It allows one to use it for broadband frequency conversion tunable both in the deep UV to visible spectral range [31,32] and ultrashort pulse diagnostics [33,34]. It has been found that NPC SBO demonstrates super-noncritical phase-matching behavior both on an angular and spectral scale [35]. This is important for conversion of broadband femtosecond radiation. Studies of femtosecond pulse conversion in NPCs are rather numerous [15,36–38]; however, currently unveiled complex spatial–temporal couplings ascribed to CND [38] must play a key role in understanding this phenomenon. In this paper we report detailed studies on CND of femtosecond pulses in 1D NPC of SBO in the frequency and time domains.

2. EXPERIMENTAL SETUP

The scheme of the experiments is shown in Fig. 1. The experimental setup consists of two stages to measure spatial and temporal features of generated SH radiation via CND. The first stage includes a femtosecond Ti:sapphire oscillator (Spectra-Physics, Tsunami) delivering nearly transform-limited pulses with a duration of about 80 fs at a repetition rate of 82 MHz. The sample under study was a NPC of SBO with the dimensions 6 mm × 3.5 mm × 3.8 mm along the crystallographic

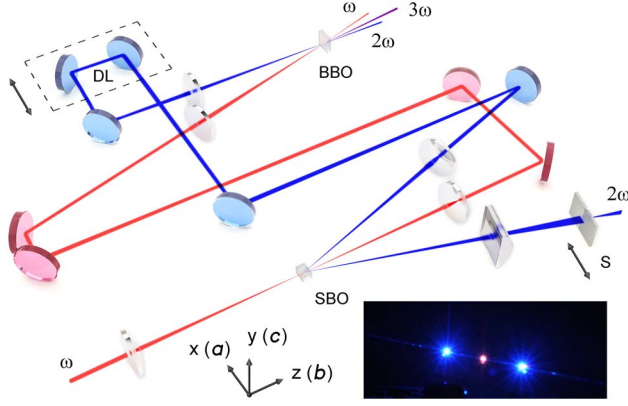


Fig. 1. Experimental setup for studying CND in the frequency (lower stage) and time (upper stage) domains (S, adjustable-width slit; DL, delay line). Domain walls lie in the crystallographic plane bc . Inset (bottom right): CND pattern on the screen.

axes a , b , and c , respectively. The sample contained a sequence of as-grown domains with walls normal to the direction of crystallographic axis a . The sample under study was mounted on a translation stage with the capability of rotation in a horizontal plane around the c axis. Fundamental radiation with average power up to 820 mW was directed along the b axis of the SBO either without focusing or with focusing by a 10 or 5 cm lens. When the fundamental wave propagated in the plane of domain walls, two SH beams were emitted symmetrically with respect to the direction of the fundamental beam. Polarization of the fundamental wave coincided with the polar crystallographic axis c to utilize the maximum nonlinear coefficient d_{ccc} of the SBO. Polarization of the SH beams was verified to be along the c axis, too. The generated SH radiation was focused in the vertical plane by a 10 cm cylindrical lens. It enables one to collect the overall radiation into the entrance of the micro-objective mounted on the fiber linked to a spectrometer. To measure spatial features of generated SH radiation, an adjustable-width slit was placed in the focal plane 60 cm away from the sample. The slit width was 20 μm . The FF and SH radiations were separated due to the noncollinear phase-matching condition. The second stage includes a variable delay line with a spatial resolution of 2.5 μm and 0.1 mm thick Type-I beta barium borate (β -BBO) crystal cut for cross-correlation measurements of the SH pulse duration. Averaged power of the SH and third harmonic (TH) was measured by a 918D power meter (Newport). Spectra were measured by Solar TII (MSDD1000) and Ocean Optics (USB4000, HR4000, and Maya 2000Pro) spectrometers, which were precisely calibrated prior to measurements.

3. THEORETICAL MODEL

Our analysis is based on the classical Akhmanov spectral amplitude formalism recently modified by Shutov *et al.* [36] for the case of CND of ultrashort pulses in a periodical nonlinear grating. Any random 1D nonlinear grating can be considered as a superposition of several regular ones contributing to CND. This assumption is expected to be correct because a finite number of domains are illuminated by a tightly focused fundamental beam under our experimental conditions. Additionally, transverse tuning the domain structure with respect to the fundamental beam is expected to allow us to use a predominant RLV that contributes to CND within the FF spot.

Thus, without considerable loss of generality, a real random domain structure should be described as a specific regular one regardless of residual contributions of other RLVs, as well as of domain walls. It is also known that the wave vectors of FF and SH under the NBD condition in NPC satisfy the general vectorial phase-matching condition [28] in the form $2\mathbf{k}_1 + \mathbf{G}_m + \Delta\mathbf{k} = \mathbf{k}_2$, where \mathbf{k}_1 and \mathbf{k}_2 are wave vectors of the FF and SH, $\Delta\mathbf{k}$ is the phase mismatch vector, and $\mathbf{G}_m = m\mathbf{G}_0$ is an RLV with m being the integer order of the primary RLV $\mathbf{G}_0 = 2\pi/\Lambda$ (Λ is the period of second-order nonlinear susceptibility modulation). A corresponding phase-matching diagram for NBD is presented in Fig. 2. This relation can be split into independent parts, namely, into the longitudinal and transverse components. The longitudinal components result in the well-known CND condition $k_2 \cos \theta_2 = 2k_1$, with θ_2 being the internal CND angle between FF and SH waves. Thus, SH radiation emits under the internal CND angle (in the crystal)

$$\theta_2 = \arccos(n_1/n_2), \quad (1)$$

where n_1 and n_2 mark the refractive indices of the FF and SH waves [39], respectively. For the transverse ones, the general relation reduces to $k_2 \sin \theta'_2 = G_m$, which is known as the condition for nonlinear Raman-Nath diffraction [40]. When these conditions are simultaneously accomplished, an efficient NBD takes place [28,30]. For the calculations, the examined configuration was specified as follows. The fundamental beam with a focal spot diameter w_0 (at the half-intensity point) propagates along the z axis (b axis of SBO), as depicted in Fig. 1. The second-order nonlinear susceptibility of the SBO material is spatially modulated in the direction of the x axis (a axis of SBO). Then, under the assumption of undepletion of the fundamental wave and the slowly varying amplitude approximation for the SH wave, the SH field amplitude is governed by the wave equation [36]:

$$\left(\frac{\partial}{\partial z} + \frac{1}{u_2} \frac{\partial}{\partial t} + \frac{i}{2k_2} \frac{\partial^2}{\partial x^2} \right) A_2(t, z, x) = -ig(x)\beta_2 A_1^2 F^2(x) F_1^2(t, z) \exp(i\Delta kz), \quad (2)$$

where $\Delta k = k_2 - 2k_1$ is the phase mismatch between SH and FF waves, A_1 is the maximum FF field amplitude, $F(x) = \exp(-x^2/a^2)$ and $F_1(t, z) = \exp(-(t - z/u_1)^2/\tau^2)$ are the transverse spatial and longitudinal spatiotemporal profiles of the FF pulse field, respectively, 2τ and $2a = w_0(2/\ln 2)^{1/2}$ are the pulse width and the focal spot diameter at the $1/e$ -field strength point, $u_{1,2}$ are the FF and SH pulse group velocities, and $\beta_2 = 2\pi k_2 \chi^{(2)}/n_2^2$ is the nonlinear coupling coefficient.

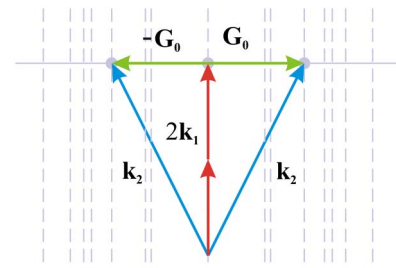


Fig. 2. Phase-matching diagram for NBD.

The function $g(x)$ responsible for $\chi^{(2)}$ modulation is equal to 1 for “positive” domains and -1 for “negative” ones. The second and third terms in the left-hand part of Eq. (2) account for the group velocity dispersion and the CND effect, respectively. By using the Fourier transformation, the solution of Eq. (2) can be expressed through its Fourier spectrum as a spectral amplitude $A(\Omega, K, z)$. Thus, the expression for the spectral intensity of the SH $S(\Omega, K, z) = |A(\Omega, K, z)|^2$ can be written in our case as follows [36]:

$$S(\Omega, K, z) = (|\alpha z|)^2 \exp\left(-\frac{\Omega^2 \tau^2}{4}\right) \times \text{sinc}\left(\frac{z}{2}\left(\Delta k + \nu\Omega - \frac{K^2}{2k_2}\right)\right)^2 R(K, a), \quad (3)$$

where $\alpha = \Gamma \tau a^2 (\pi/2)^{1/2}$, $\Gamma = -i\beta_2 I_1$, $R(K, a) = (\sum_m g_m \exp(-a^2(mG_0 + K)^2/8))^2$, Ω is the frequency detuning from the central doubled frequency of the fundamental wave, $\nu = (1/u_2 - 1/u_1)$ is the group velocity mismatch, K and G_0 are the spatial frequency and the primary RLV provided by the NPC structure, respectively, and g_m is the Fourier amplitude corresponding to the RLV with the integer index m . The spatial frequency K and the internal SH propagation angles are connected by $K = 4\pi n_2 \sin(\theta_2)/\lambda$, with λ being the fundamental wavelength. In calculations, the value of the primary RLV is determined by using the expression $G_0 = \gamma K$, with K taken for the central FF wavelength, and γ is a variable parameter with $\gamma = 1$ corresponding to the exact phase matching for the central FF wavelength.

4. RESULTS AND DISCUSSION

The solution for the SH spectral intensity [Eq. (3)] is the product of three functions, namely, the sinc function, $R(K, a)$, and the Gaussian spectral density envelope factor corresponding to the fundamental beam. These functions are plotted in Fig. 3(a) for the central fundamental wavelength 800 nm and the fundamental spot size at the half-intensity point $w_0 = 40 \mu\text{m}$, corresponding to the focusing by a 10 cm lens. Instead of areal random structure, the periodic structure was used with the RLV value $G_0 = 4.563 \mu\text{m}^{-1}$, exactly corresponding to the first order of CND at 800 nm ($\gamma = 1$). In the calculations we also used the measured fundamental pulse duration of 80 fs and the nonlinear interaction length $z = 3.5 \text{ mm}$, equal to the thickness of the sample. Combining these functions results in the complex spatial behavior of a generated SH spectrum [Fig. 3(b)]. At the same time, the angular dependence integrated over the spectrum and the spectral dependence integrated over the angle are smooth, as shown in the projections on the coordinate planes in Fig. 3(b). The main feature of this dependence is the presence of sidebands arising from the Čerenkov phase-matching condition. Therefore, integral and local SH spectra, i.e., the overall spectrum within a small angle, should be distinguished. Both these sidebands and the local SH spectra may be proved by angular scanning with the help of a narrow-width slit. Another feature is the angular chirp experimentally observed in [37,38] that can be understood in terms of the strong spectral dependence of the CND angle (e.g., see [16,17,37,38]). The sinc function in Eq. (3) is responsible for this spectral behavior. Under experimental conditions, calculated angular chirp was $-0.033 \text{ deg}\cdot\text{nm}^{-1}$. The CND angle for the maximum of the

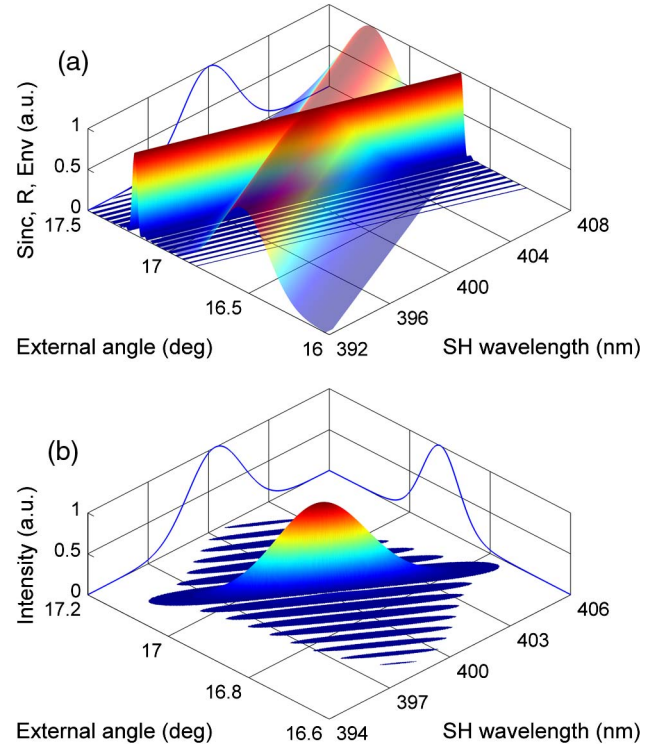


Fig. 3. (a) Sinc function in Eq. (3), the normalized Fourier transform $R(K, a)$ (semi-transparent), and the Gaussian envelope factor (solid line) in angle/wavelength coordinates; (b) resulting function $S(\Omega, K, z)$ and its projections to the angular and spectral coordinates. Data are presented in the range down to -30 dB for clarity.

SH intensity profile obtained using Eq. (3) was 16.94 deg, which slightly differs from the value 16.95 deg calculated using Eq. (1) and converting the internal angle to the external one. Note that our calculations give the chirp-free SH radiation at the fundamental wavelength of $1.2 \mu\text{m}$ for SBO.

It has experimentally been found that the spectral features of generated radiation are very sensitive to the fundamental beam spot size. Two regimes of the SH generation (SHG) were used in the experiments. The first one occurs without focusing the fundamental radiation into the NPC. In that case multiple overlapping beams were observed during scanning of the fundamental beam in the direction along the crystallographic axis a . These beams originate from CND in different parts of the domain structure within the fundamental beam spot and require different RLVs. This leads to the complex spectrogram of SH with narrow spectral peaks and weak dependence on the coordinate [Fig. 4(a)]. On the other hand, when the fundamental radiation is focused into the NPC with either a 5 or 10 cm lens, solitary SH beams are observed. The intensity profiles of these beams are well fitted by the Gaussian function in both transverse directions. In this case, transverse scanning of the fundamental beam within the NPC results in dependence of the SH spectrum on the beam position that consists of sharp peaks with a wider spectral width [Fig. 4(b)]. These findings support recent theoretical results obtained in [41]. A comparison of dependences in Figs. 4(a) and 4(b) shows that the positions of the maximum peaks nearly coincide. Maximal SHG efficiency in two beams was up to 2.11% ($2.58\% \cdot \text{W}^{-1}$), which is the highest value reported so far for CND from a high-repetition-rate femtosecond

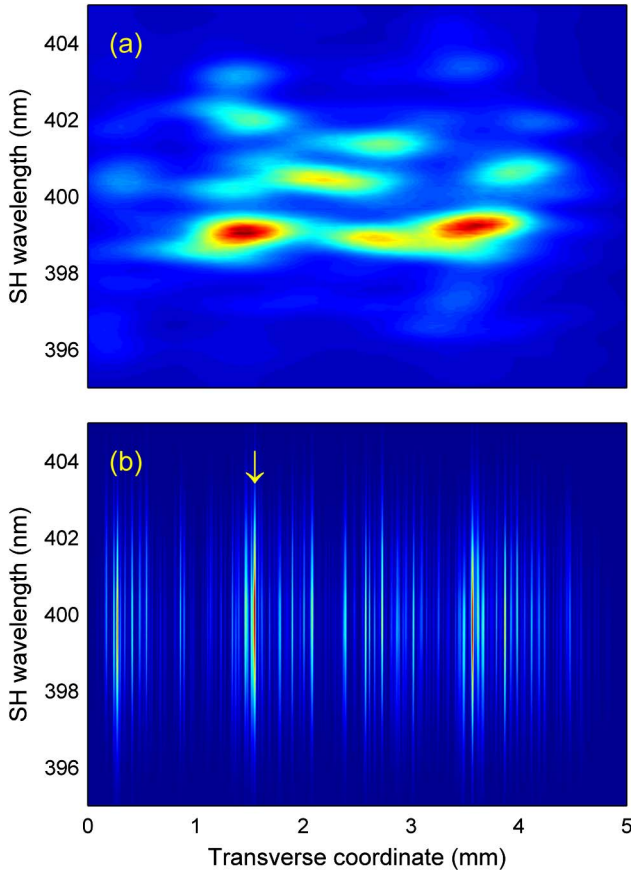


Fig. 4. Measured SH spectrograms (a) without focusing and (b) with focusing by a 5 cm lens. The transverse spatial pitch is (a) 50 μm and (b) 1.25 μm . The vertical arrow indicates the fundamental beam position used in the following experiments.

oscillator. Then we carried out experiments to observe the spatial dependence of the local SH spectrum within the beam cross section. These experiments were done when the fundamental beam position was tuned to the maximum of the SH power marked in Fig. 4(b). We also observed a weak SH signal uniformly distributed in the horizontal plane, which is believed to be attributed to nonlinear Raman–Nath diffraction [42] of femtosecond pulses in thick random NPC (Fig. 1, inset).

As shown in Fig. 5(a), the measured SH spectrum demonstrates the frequency shift 25 cm^{-1} down to lower frequencies with focusing of the fundamental beam by a 10 cm lens. This is also predicted by the theoretical model used when the wave vector mismatch is strictly compensated by RLV [Fig. 5(b)], resulting in NBD. The origin of this shift is seen from Figs. 3(a) and 3(b), where resulting spectral dependence [Fig. 3(b)] is formed by the combined action of the sinc term, the Fourier transform of the nonlinear susceptibility function, and the Gaussian spectral density envelope [Fig. 3(a)]. It is worth noting that the spectrum of the fundamental radiation from the mode-locked oscillator used is expected to be well described by the sech^2 function instead of the Gaussian shape assumed in the calculations. However, in the calculations this spectrum was approximated as the Gaussian, because the corresponding solution for the sech^2 profile can not be performed analytically. Good agreement between measured and calculated SH spectra is evident. Since the frequency shift

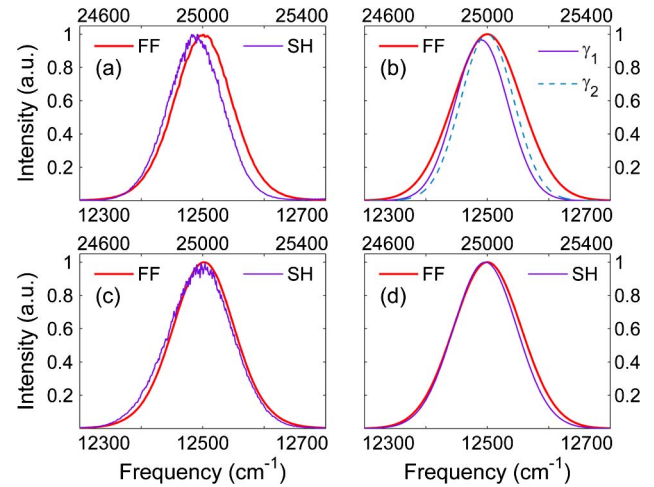


Fig. 5. (a), (c) Measured and (b), (d) calculated spectra of the SH (violet) and squared spectra of the FF (red) radiation for focusing by a 10 cm (top row) and 5 cm (bottom row) lens (with $\gamma_1 = 1$; $\gamma_2 = 1.0035$). The upper scale corresponds to the SH spectrum. The movie (Media 1) refers to (b).

evident in Fig. 5(a) may influence the integral conversion efficiency, we considered the dependence of the SH spectrum on the RLV value, i.e., parameter γ . As demonstrated by the movie (Media 1), for RLV variations in the range of 1%–2% from the exact NBD value ($\gamma = 1$), the SH spectrum keeps its shape but experiences a frequency shift. Larger deviations of the RLV value lead to modification of the SH spectrum shape and reduce the conversion efficiency. This shift is canceled out by choosing the RLV value $\gamma = 1.0035$ [Fig. 5(b)]. For this value the external SH propagation angle 16.95 deg becomes equal to that calculated using Eq. (1). In this case, the SHG efficiency has a maximum, and the SHG efficiency increases by 3.6% with respect to that expected for exact phase matching at the central spectral component of FF. The high sensitivity of the SH spectral maximum to the RLV may be used for nondestructive RLV diagnostics of NPC structures. Another feature of CND in an NPC is the influence of the fundamental beam spot size on the SH spectrum width. As shown in Fig. 5(a), the SH spectrum is narrower than the squared fundamental one. It is commonly known that the conversion of the broadband femtosecond pulses for any cases of phase matching requires suitable spectral bandwidth of the nonlinear converter, and the thickness of a nonlinear medium must be as small as possible because of the walk-off between the FF and SH pulses due to the different group velocities. The latter is the main physical reason for the narrowing of the SH spectrum in comparison with the squared fundamental one. However, in the case of CND, this narrowing can be reduced with tight focusing of the FF beam. Indeed, the spectral intensity $S(\Omega, K, z)$ [see Eq. (3)] is strongly affected by the $R(K, a)$ function characterizing the influence of the quadratic nonlinear susceptibility modulation. The width of the $R(K, a)$ function is determined by the beam spot size a and increases with decreasing a . We experimentally proved this assumption by replacing the 10 cm lens with a 5 cm one. After this change the NPC position was adjusted along the a axis to the same position indicated in Fig. 4(b) by tuning the SH power to the maximum. In that case the spectrum of the SH fits well with the squared fundamental

spectrum, as shown in Fig. 5(c). The calculated curves in Fig. 5(d) show that in the case of the 5 cm lens almost complete reproduction of the FF spectrum in the SH one is possible, while in case of the 10 cm lens it is impossible for any G_0 . The decrease in the FF beam spot also leads to the reduction of the frequency shift down to 6 cm^{-1} . Note that the calculated intensity of the SH is increased by 4.9 times with respect to the case of focusing by the 10 cm lens and the RLV value $G_0(\gamma = 1.0035)$, due to both the larger fundamental wave intensity and the wider spectral acceptance. Therefore, in order to utilize the spectral bandwidth of the envelope function of the fundamental radiation, the beam width of the fundamental wave should be as small as possible. Calculations show that with the decrease in the beam spot, the spectral shift asymptotically approaches zero and the spectral width of the SH becomes the maximum. With the increase in the beam spot, the shift increases in the vicinity of the top of the FF spectrum, but finally, at the slope of the Gaussian FF spectral function, the shift saturates (in our conditions at 48 cm^{-1}), while the SH spectrum becomes more and more narrow.

Measurements of the SH spectrum distribution across the beam section were performed by using an adjustable-width slit. Our study began with an investigation of the SH spectrum as dependent on the slit width. The SH spectrum is revealed to become narrower during slit narrowing, as depicted in Fig. 6. The full width at half-maximum (FWHM) of the SH spectrum converges to the minimum of 1.1 nm in the manner shown in Fig. 6. This value slightly differs from the expected one, which is 1.15 nm. The main characteristics contributing to the calculated width of the central peak of the local SH spectrum are dispersion of the SBO crystal and the nonlinear interaction length z , which is set to be 3.5 mm. The calculated FWHM of the spectrum of the SH radiation may be adjusted to the experimental one by setting a nonlinear interaction length of 3.75 mm.

The local SH spectra were recorded during the scanning of the slit position at the spatial pitch of $50 \mu\text{m}$ in the horizontal transverse direction. The slit width was chosen to be $20 \mu\text{m}$, which is equivalent to the angular interval 0.033 mrad . Measured spectra were averaged within this angular interval. No noticeable spectral distortions due to diffraction at the slit are expected, as verified by calculations. A series of local SH

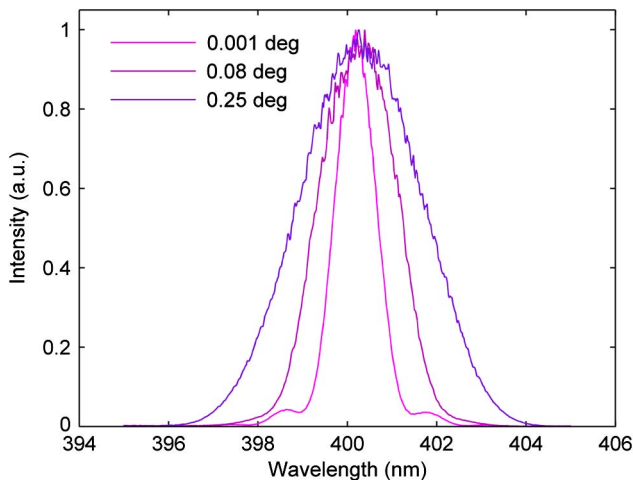


Fig. 6. Measured SH spectra at different slit widths.

spectra at different angular positions of the slit are plotted in Fig. 7. One can see that spectral components are nonuniformly distributed across the beam section and secondary maxima appear for high angles of propagation. Corresponding calculated local spectra of the SH are also presented in Fig. 7. The calculations show that these maxima are due to the sinc function in Eq. (3), not the $R(K, a)$ function that is responsible for the influence of the NPC structure. However, the relative magnitudes of these maxima are affected by the combined action of the RLV employed, the fundamental beam spot size, and the FF spectral bandwidth. The results of the calculations are found to be very sensitive to the input data. The following data were used in the calculation: an FF central wavelength of 800 nm, an FF pulse duration of 80 fs, an FF beam spot size of $38 \mu\text{m}$ and an interaction length of $3750 \mu\text{m}$ (slightly higher than the thickness of the sample). Instead of a real random structure, a periodic structure was used with the RLV $G_0(\gamma = 1) = 4.653 \mu\text{m}^{-1}$, exactly corresponding to the first order of CND at 800 nm. The corresponding angles for the calculated spectra in Fig. 7 were corrected by a factor of 1.13 to obtain the best fit with the experimental data. We ascribe the existence of this factor to the divergence of the SH beam, which was experimentally found to be larger than the diffraction-limited one. As a result, the measured and calculated local spectra coincide fairly well for small deflection angles, but the correlation is worse for larger angles, as demonstrated by the movie (Media 2). There are two reasons of this discrepancy. The first one is the fact that the spectrum of the fundamental radiation is better described by the sech^2 function instead of the Gaussian shape used in the calculation, as discussed above. The difference between these functions becomes significant with the detuning of the current frequency from the doubled central frequency of the fundamental radiation. It results in the divergence between the measured and calculated local SH spectra for high propagation angles where the signal is complex and becomes weaker. Another reason is the residual cw output of the laser and, as a consequence, noise background (less than 0.2%) as supported by our spectral measurements. For the calculations presented in Fig. 7 and the corresponding movie, the constant background ($15 \cdot 10^{-3}$) was introduced to the FF envelope function.

Figure 8 shows the resulting angular dependences of the SH spectrum for two specific cases of focusing by a 5 cm and a 10 cm lens. These dependences demonstrate the angular chirp and secondary maxima as shown in Fig. 3(b). There is some difference between the measured (16.70 deg) and calculated CND angles (16.95 deg) that can be assigned to the refractive index approximation uncertainty. The measured angular chirp was $-0.036 \text{ deg} \cdot \text{nm}^{-1}$, in good agreement with the calculated one magnified by a factor of 1.13 as explained above ($-0.037 \text{ deg} \cdot \text{nm}^{-1}$). Similar scanning of the slit along the vertical transverse direction (normal to the RLV plane) showed no angular changes in the SH spectra.

The fact that SH radiation possesses the angular chirp indicates the presence of the complex spatial-temporal coupling [43] of the SH radiation obtained via CND. After collimating the SH beam, the angular chirp is mostly compensated. Dominating the spatial-temporal coupling after the lens is the spatial chirp that leads to a decrease in the local spectrum width, and an increase in the pulse duration is expected.

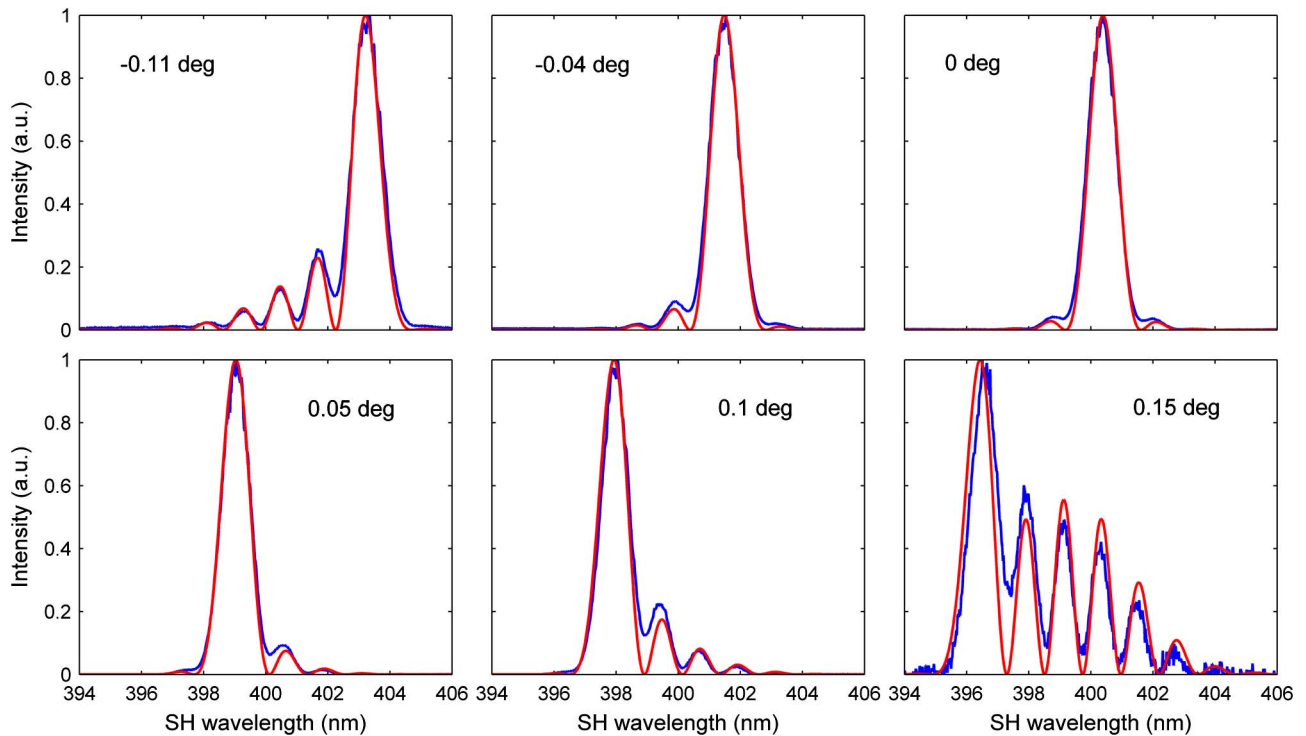


Fig. 7. Series of measured (blue) and calculated (red) local SH spectra for the slit position varies from -0.1 to 0.15 deg. The movie ([Media 2](#)) shows the variation of the local SH spectrum with slit position.

This increase can be tested via cross-correlation measurement. The earlier study showed satisfactory agreement between the measured pulse duration and the local spectrum

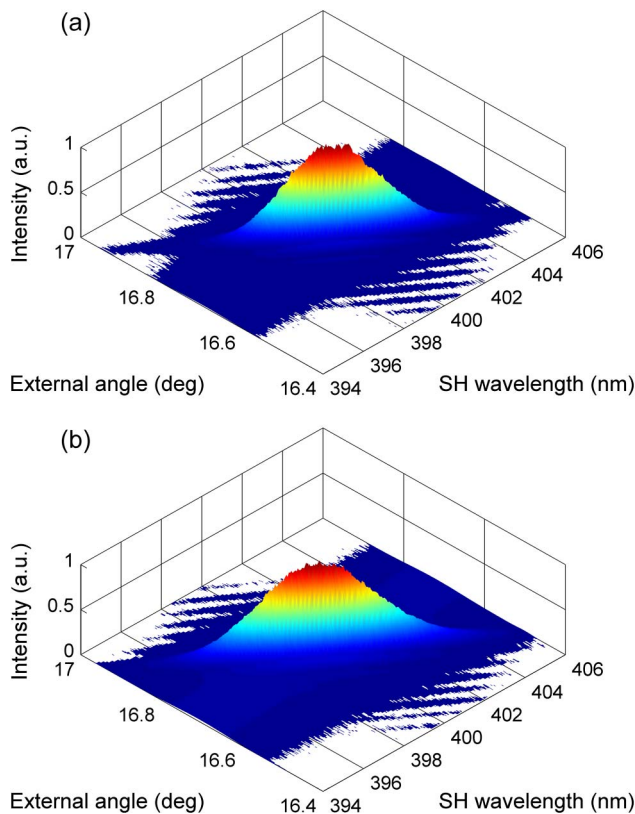


Fig. 8. Measured SH spectra on the slit position with focusing by (a) a 10 cm and (b) a 5 cm lens. The background was excluded.

width [38]. However, the measured pulse duration was slightly lower (170–200 fs) than one would expect from the local spectral bandwidth (215 fs). The experiments were performed using the Type-I BBO crystal cut for cross-correlation measurements of the SH pulse duration ($\theta_{ooe} = 52.4$ deg). The main advantage of the vectorial phase matching employed is the spectral dependence of the angle of the emitted sum frequency signal that may be used to measure chirped femtosecond pulses. The small thickness of the sample provides the desired spectral bandwidth and reduces the group velocity dispersion effect. Unfortunately, the measured TH signal was too weak for direct measurements using a power meter. Therefore, we used a spectrometer with a high-accumulation-time mode to record the TH spectra in the course of the cross-correlation procedure. These results are presented in Fig. 9.

As is clearly seen, the measured cross-correlation function is well fitted by the Gaussian function in the -10 dB range instead of the sech^2 pulse profile corresponding to the FF spectrum. This supports the assumption that the SH pulse duration is mainly determined by the local spectrum width, but not the full spectral bandwidth, because $\text{sinc}^2(x) \propto \exp(-\alpha x^2)$ with $\alpha = 0.36$. The FWHM of the cross-correlation function presented in Fig. 9(b) was 215 fs. Thus, the retrieved SH pulse FWHM is close to 200 fs. The measured cross-correlation trace contains background. It is expected that the origin of this background is introduced by inherent characteristics of the femtosecond oscillator, as supported by the measured fundamental spectra. Side wings observed within the -10 to -20 dB range are believed to be attributed to experimental inaccuracy. Good agreement between the measured cross-correlation function and its Gaussian fit means good quality of the temporal shape of the SH pulses.

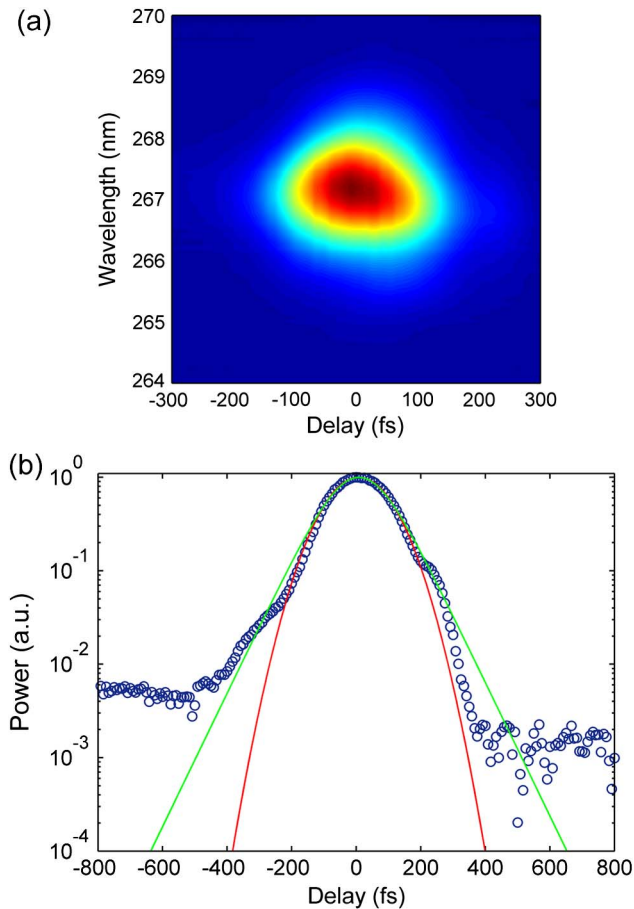


Fig. 9. (a) Measured TH spectrum as a function of delay between the FF and SH pulses and (b) measured cross-correlation function (circles) fitted by the Gaussian (red) and sech^2 (green) functions.

5. CONCLUSION

We studied CND of femtosecond pulses in a 1D NPC of SBO in both the frequency and time domains. Spectral features of SH radiation were measured in the course of mapping the NPC structure. The SH spectrum dramatically changes with both the transverse position of the fundamental beam within the NPC structure and the fundamental beam spot size. These results are specific for a highly randomized 1D NPC structure of SBO and strongly differ from those obtained with any other known NPCs. The spectral width of the SH radiation is found to be fundamental beam size dependent, and optimal focusing should be used for exact conversion of the fundamental spectrum into the SH one. The local SH spectrum demonstrates complex angular behavior within the beam cross section. The experimental results are in excellent agreement with the calculations. The maximum SHG efficiency was up to 2.1% with pumping by a femtosecond oscillator.

ACKNOWLEDGMENTS

The work was partially supported by the Grant of the President of the Russian Federation MK-250.2013.2, by RFBR through Grant No. 12-02-31167, by the Ministry of Education and Science of the Russian Federation (Contract No. 14.B37.21.0730), by Krasnoyarsk Regional Fund of Science and Technical Activity Support, by PSB RAS Project 2.5.2, and by SFU Grant F12.

REFERENCES

1. V. Berger, "Nonlinear photonic crystals," *Phys. Rev. Lett.* **81**, 4136–4139 (1998).
2. H. X. Li, S. Y. Mu, P. Xu, M. L. Zhong, C. D. Chen, X. P. Hu, W. N. Cui, and S. N. Zhu, "Multicolor Čerenkov conical beams generation by cascaded- $\chi^{(2)}$ processes in radially poled nonlinear photonic crystals," *Appl. Phys. Lett.* **100**, 101101 (2012).
3. N. An, H. Ren, Y. Zheng, X. Deng, and X. Chen, "Čerenkov high-order harmonic generation by multistep cascading in $\chi^{(2)}$ nonlinear photonic crystal," *Appl. Phys. Lett.* **100**, 221103 (2012).
4. L. Mateos, P. Molina, J. Galisteo, C. López, L. E. Bausá, and M. O. Ramírez, "Simultaneous generation of second to fifth harmonic conical beams in a two dimensional nonlinear photonic crystal," *Opt. Express* **20**, 29940–29948 (2012).
5. Y. Zhang, Z. D. Gao, Z. Qi, S. N. Zhu, and N. B. Ming, "Nonlinear Čerenkov radiation in nonlinear photonic crystal waveguides," *Phys. Rev. Lett.* **100**, 163904 (2008).
6. Y. Sheng, V. Roppo, M. Ren, K. Kalinowski, C. Cojocaru, J. Trull, Z. Li, K. Koynov, and W. Krolikowski, "Multi-directional Čerenkov second harmonic generation in two-dimensional nonlinear photonic crystal," *Opt. Express* **20**, 3948–3953 (2012).
7. M. B. Nasr, S. Carrasco, B. E. A. Saleh, A. V. Sergienko, M. C. Teich, J. P. Torres, L. Torner, D. S. Hum, and M. M. Fejer, "Ultrabroadband biphotons generated via chirped quasi-phase-matched optical parametric down-conversion," *Phys. Rev. Lett.* **100**, 183601 (2008).
8. G. Brida, M. V. Chekhova, I. P. Degiovanni, M. Genovese, G. Kh. Kitaeva, A. Meda, and O. A. Shumilkina, "Chirped biphotons and their compression in optical fibers," *Phys. Rev. Lett.* **103**, 193602 (2009).
9. G. K. Kitaeva, "Terahertz generation by means of optical lasers," *Laser Phys. Lett.* **5**, 559–576 (2008).
10. A. Shapira, R. Shiloh, I. Juwiler, and A. Arie, "Two-dimensional nonlinear beam shaping," *Opt. Lett.* **37**, 2136–2138 (2012).
11. I. Freund, "Nonlinear diffraction," *Phys. Rev. Lett.* **21**, 1404–1406 (1968).
12. P. K. Tien, R. Ulrich, and R. J. Martin, "Optical second harmonic generation in form of coherent Čerenkov radiation from a thin-film waveguide," *Appl. Phys. Lett.* **17**, 447–450 (1970).
13. C. Chen, J. Su, Y. Zhang, P. Xu, X. Hu, G. Zhao, Y. Liu, X. Lv, and S. Zhu, "Mode-coupling Čerenkov sum-frequency-generation in a multimode planar waveguide," *Appl. Phys. Lett.* **97**, 161112 (2010).
14. A. A. Kaminskii, H. Nishioka, K. Ueda, W. Odajima, M. Tateno, K. Sasaki, and A. V. Butashin, "Second-harmonic generation with Čerenkov-type phase matching in a bulk nonlinear LaBGeO_5 crystal," *Quantum Electron.* **26**, 381–382 (1996).
15. R. Fischer, S. M. Saltiel, D. N. Neshev, W. Krolikowski, and Yu. S. Kivshar, "Broadband femtosecond frequency doubling in random media," *Appl. Phys. Lett.* **89**, 191105 (2006).
16. P. Molina, M. de la O Ramírez, and L. E. Bausá, "Strontium barium niobate as a multifunctional two-dimensional nonlinear 'photonic glass,'" *Adv. Funct. Mater.* **18**, 709–715 (2008).
17. P. Molina, S. Álvarez-García, M. O. Ramírez, J. García-Solé, L. E. Bausá, H. Zhang, W. Gao, J. Wang, and M. Jiang, "Nonlinear prism based on the natural ferroelectric domain structure in calcium barium niobate," *Appl. Phys. Lett.* **94**, 071111 (2009).
18. M. Ayoub, J. Imbrock, and C. Denz, "Second harmonic generation in multi-domain χ^2 media: from disorder to order," *Opt. Express* **19**, 11340–11354 (2011).
19. M. Ayoub, P. Roedig, J. Imbrock, and C. Denz, "Domain-shape-based modulation of Čerenkov second-harmonic generation in multidomain strontium barium niobate," *Opt. Lett.* **36**, 4371–4373 (2011).
20. M. Ayoub, P. Roedig, J. Imbrock, and C. Denz, "Cascaded Čerenkov third-harmonic generation in random quadratic media," *Appl. Phys. Lett.* **99**, 241109 (2011).
21. S. I. Bozhevolnyi, J. M. Hvam, K. Pedersen, F. Laurell, H. Karlsson, T. Skettrup, and M. Belmonte, "Second harmonic imaging of ferroelectric domain walls," *Appl. Phys. Lett.* **73**, 1814–1816 (1998).
22. A. Fragemann, V. Pasiskevicius, and F. Laurell, "Second-order nonlinearities in domain walls of periodically poled KTiOPO_4 ," *Appl. Phys. Lett.* **85**, 375–377 (2004).

23. K. Kalinowski, Q. Kong, V. Roppo, A. Arie, Y. Sheng, and W. Krolikowski, "Wavelength and position tuning of Čerenkov second-harmonic generation in optical superlattice," *Appl. Phys. Lett.* **99**, 181128 (2011).
24. Y. Sheng, V. Roppo, K. Kalinowski, and W. Krolikowski, "Role of a localized modulation of $\chi^{(2)}$ in Čerenkov second-harmonic generation in nonlinear bulk medium," *Opt. Lett.* **37**, 3864–3866 (2012).
25. H. Ren, X. Deng, Y. Zheng, N. An, and X. Chen, "Nonlinear Čerenkov radiation in an anomalous dispersive medium," *Phys. Rev. Lett.* **108**, 223901 (2012).
26. X. Deng and X. Chen, "Domain wall characterization in ferroelectrics by using localized nonlinearities," *Opt. Express* **18**, 15597–15602 (2010).
27. Y. Sheng, A. Best, H. J. Butt, W. Krolikowski, A. Arie, and K. Koynov, "Three-dimensional ferroelectric domain visualization by Čerenkov-type second harmonic generation," *Opt. Express* **18**, 16539–16545 (2010).
28. S. M. Saltiel, D. N. Neshev, R. Fischer, W. Krolikowski, A. Arie, and Y. S. Kivshar, "Generation of second-harmonic conical waves via nonlinear Bragg diffraction," *Phys. Rev. Lett.* **100**, 103902 (2008).
29. A. Shapira and A. Arie, "Phase-matched nonlinear diffraction," *Opt. Lett.* **36**, 1933–1935 (2011).
30. K. Kalinowski, P. Roedig, Y. Sheng, M. Ayoub, J. Imbrock, C. Denz, and W. Krolikowski, "Enhanced Čerenkov second-harmonic emission in nonlinear photonic structures," *Opt. Lett.* **37**, 1832–1834 (2012).
31. A. S. Aleksandrovsky, A. M. Vyunishev, A. I. Zaitsev, and V. V. Slabko, "Random quasi-phase-matched conversion of broadband radiation in a nonlinear photonic crystal," *Phys. Rev. A* **82**, 055806 (2010).
32. A. S. Aleksandrovsky, A. M. Vyunishev, V. V. Slabko, A. I. Zaitsev, and A. V. Zamkov, "Tunable femtosecond frequency doubling in random domain structure of strontium tetraborate," *Opt. Commun.* **282**, 2263–2266 (2009).
33. A. S. Aleksandrovsky, A. M. Vyunishev, A. I. Zaitsev, A. A. Ikonnikov, and G. I. Pospelov, "Ultrashort pulses characterization by nonlinear diffraction from virtual beam," *Appl. Phys. Lett.* **98**, 061104 (2011).
34. A. S. Aleksandrovsky, A. M. Vyunishev, A. I. Zaitsev, G. I. Pospelov, and V. V. Slabko, "Diagnostics of fs pulses by nonlinear random quasi-phase-matched frequency doubling," *Appl. Phys. Lett.* **99**, 211105 (2011).
35. A. S. Aleksandrovsky, A. M. Vyunishev, and A. I. Zaitsev, "Applications of random nonlinear photonic crystals based on strontium tetraborate," *Crystals* **2**, 1393–1409 (2012).
36. I. V. Shutov, I. A. Ozheredov, A. V. Shumitski, and A. S. Chirkin, "Second harmonic generation by femtosecond laser pulses in the Laue scheme," *Opt. Spectrosc.* **105**, 79–84 (2008).
37. X. Deng, H. Ren, H. Lao, and X. Chen, "Research on Čerenkov second-harmonic generation in periodically poled lithium niobate by femtosecond pulses," *J. Opt. Soc. Am. B* **27**, 1475–1480 (2010).
38. A. M. Vyunishev, A. S. Aleksandrovsky, A. I. Zaitsev, and V. V. Slabko, "Čerenkov nonlinear diffraction in random nonlinear photonic crystal of strontium tetraborate," *Appl. Phys. Lett.* **101**, 211114 (2012).
39. Yu. S. Oseledchik, A. L. Prosvirmin, A. I. Pisarevskiy, V. V. Starshenko, V. V. Osadchuk, S. P. Belokrys, N. V. Svitanko, A. S. Korol, S. A. Krikunov, and A. F. Selevich, "New nonlinear optical crystals: strontium and lead tetraborates," *Opt. Mater.* **4**, 669–674 (1995).
40. S. M. Saltiel, D. N. Neshev, W. Krolikowski, A. Arie, O. Bang, and Y. S. Kivshar, "Multiorder nonlinear diffraction in frequency doubling processes," *Opt. Lett.* **34**, 848–850 (2009).
41. Y. Sheng, Q. Kong, V. Roppo, K. Kalinowski, Q. Wang, C. Cojocar, and W. Krolikowski, "Theoretical study of Čerenkov-type second-harmonic generation in periodically poled ferroelectric crystals," *J. Opt. Soc. Am. B* **29**, 312–318 (2012).
42. Y. Sheng, Q. Kong, W. Wang, K. Kalinowski, and W. Krolikowski, "Theoretical investigations of nonlinear Raman–Nath diffraction in the frequency doubling process," *J. Phys. B* **45**, 055401 (2012).
43. S. Akturk, X. Gu, P. Bownan, and R. Trebino, "Spatio-temporal couplings in ultrashort laser pulses," *J. Opt.* **12**, 093001 (2010).